Catalysis Science & Technology

Understanding and controlling the formation of surface anion vacancies for catalytic applications

Journal:	*Catalysis Science & Technology*
Manuscript ID	CY-PER-01-2022-000014.R2
Article Type:	Perspective
Date Submitted by the Author:	10-Mar-2022
Complete List of Authors:	Mine, Shinya; Hokkaido University, Catalysis; Osaka Prefecture University, Applied Chemistry, Graduate School of Engineering Toyao, Takashi; Hokkaido university, Institute for Catalysis Hinuma, Yoyo; AIST, Shimizu, Ken-ichi; Hokkaido University, Catalysis Research Center

Understanding and controlling the formation of surface anion vacancies for catalytic applications

Shinya Mine,[1] Takashi Toyao,[1,2] Yoyo Hinuma,[3*] Ken-chi Shimizu[1,2*]

[1] Institute for Catalysis, Hokkaido University, N-21, W-10, 1-5, Sapporo 001-0021, Japan

[2] Elements Strategy Initiative for Catalysts and Batteries, Kyoto University, Katsura, Nishigyo, Kyoto 615-8520, Japan

[3] Department of Energy and Environment, National Institute of Advanced Industrial Science and Technology (AIST), 1-8-31, Midorigaoka, Ikeda 563-8577, Japan

Abstract

Defects are important as they often govern the chemical and physical properties of solid materials. Surface defect sites, such as anion vacancies, most commonly oxygen vacancies for oxides, are well-known reaction sites in heterogeneous catalysis. Although the importance of defects at catalyst surfaces is well recognized and commonly accepted by the catalysis community, details of their atomic and electronic structures are lacking, which is largely due to the fact that identifying surface defects is challenging and mostly beyond the resolution of currently available experimental techniques. Moreover, the complexities of the geometrical and electronic structures of surfaces make computational investigations difficult. Presently, studying an individual material requires substantial amounts of experimental and calculational time/cost; hence few comprehensive studies have been performed. In this perspective, we summarize our recent systematic computational efforts using density functional theory to calculate surface anion vacancy formation energies (E_{vac}) as important descriptors of catalytic performance. The systems explored include binary oxides, complex oxides, carbides, nitrides, sulfides, hydrides, and oxides with supported metals. Exotic surfaces with high-index orientations were also considered. In addition, we studied relationships between physicochemical properties and surface anion E_{vac} values in order to rationalize the properties of compounds/surfaces and the support metals, and to provide a predictive tool. The definitive goal of our work was to gain fundamental knowledge of the factors determining surface defect formation and ultimately catalytic activity/selectivity so that ideal catalytic materials/surfaces can be designed and manipulated in a highly precise manner.

1. Introduction

The chemistry and physics of solid materials is incomplete without considering various types of defect.[1–5] Various point and extended defects introduced into a structure can dominate its reactivity, as well as its catalytic, optical, mechanical, and electrical properties.[6–10] In particular, surface point defects, such as anion vacancies, strongly affect catalytic performance in terms of both activity and selectivity.[11,12] For instance, the Mars–van Krevelen (MvK) mechanism, in which anion vacancy sites on a solid surface act as reaction sites, is a frequently encountered catalysis process.[13,14] The energy required to form such defects in the catalyst is typically used to rationalize and predict the performance of associated catalytic processes.[15]

Surface defects have been investigated using various experimental techniques for many years.[16–18] Scanning probe technology has proven to be a useful tool, providing significant amounts of information on defective surface structures, as it enables the direct visualization of surface defects.[19–22] On the other hand, experimentally observing vacancies requires sophisticated techniques; consequently, they remain largely unexplored.[23] In addition, the vacancy formation energy (E_{vac}) is not always experimentally obtainable,[23] which has led to many theoretical studies on anion vacancies in recent years.[24–32] Although many contributions toward obtaining E_{vac} values and employing them as descriptors of catalytic performance have been reported, especially for bulk systems, only a limited number of surfaces have been investigated, and no comprehensive studies have been conducted.[2,23,31] Indeed, this is a major reason for why data-science-based approaches, which have attracted much recent attention in the fields of molecular and materials science, remain in their infancies in the heterogeneous catalysis field.[33–35] While machine learning (ML), a sub-field of data science, is expected to accelerate research in terms of the time and cost involved when properly devised, the complexities of solid surfaces provide significant challenges.[33] Due to broken symmetry at the surface, atoms near the surface generally do not adopt the same positions as in the bulk and relax or reform to other structures. As Pauli once famously said: ‘‘God made the bulk; surfaces were invented by the devil’’ (**Figure 1**); hence, the complexities and varieties of surface structures compared to their bulk equivalents provide significant difficulties for obtaining clean and reliable descriptors for use in ML model constructs of surface-catalyzed reactions.

Several materials databases are currently available, including the Inorganic Crystal Structure Database (ICSD),[36] AtomWork,[37] the Materials Project,[38] the Automatic Flow of Materials Discovery Library (AFLOWLIB),[39] and the Open Quantum Materials Database (OQMD)[40] as well as surface-property/reaction databases, such as Catalysis-Hub.org[41] and the Open Catalyst Project.[42] However, these model varieties are inadequate, especially for transition-metal-containing compound surfaces due to their additional complexities and higher computational costs, despite the importance in heterogeneous catalysis. Therefore, determining E_{vac} values for various compound surfaces at the same computational level using comparable structural models is highly desirable in order to provide

meaningful comparisons. This information is particularly important for experimental researchers that require such information when designing and developing practical heterogeneous catalysts.[11]

In this sense, we have endeavored to comprehensively calculate the surface anion E_{vac} values of a variety of compounds, including relatively simple binary oxides, complex oxides, carbides, nitrides, sulfides, and hydrides, as well as oxides with supported metals at metal/oxide perimeter sites; high-index-oriented exotic surfaces were also considered. Throughout this campaign, density functional theory (DFT) calculations were performed using the Vienna Ab initio Simulation Package (VASP) code[43,44] at the same computational level (PBEsol(+U)).[45] While the PBEsol(+U) functional is not the most computationally accurate, as it underestimates bandgap (BG) values, it nevertheless captures trends at reasonable computational cost and facilitates qualitative discussion.[31,46] In addition to providing these E_{vac} values, we endeavored to correlate surface anion E_{vac} values with the physicochemical properties of compounds/surfaces with support metals by deconvoluting the observed trends into electronic structures, which is beneficial when screening catalysts (even for as-yet known materials) for specific applications without incurring significant experimental and/or computational costs. The physicochemical properties adopted as descriptors were selected from readily available sources such as the periodic table, handbooks, and public databases, and DFT calculations obtained through E_{vac} calculations because the aim of our effort is to accelerate screening of materials by estimating materials properties, which are difficult to obtain, by using easily obtainable values. This Perspective summarizes our recent computational efforts in this campaign, as well as the relevant work of others reported in the literature. Computationally assisted future catalysis research is discussed in this perspective together with the difficulties and limitations associated with the complexities of surface chemistry.

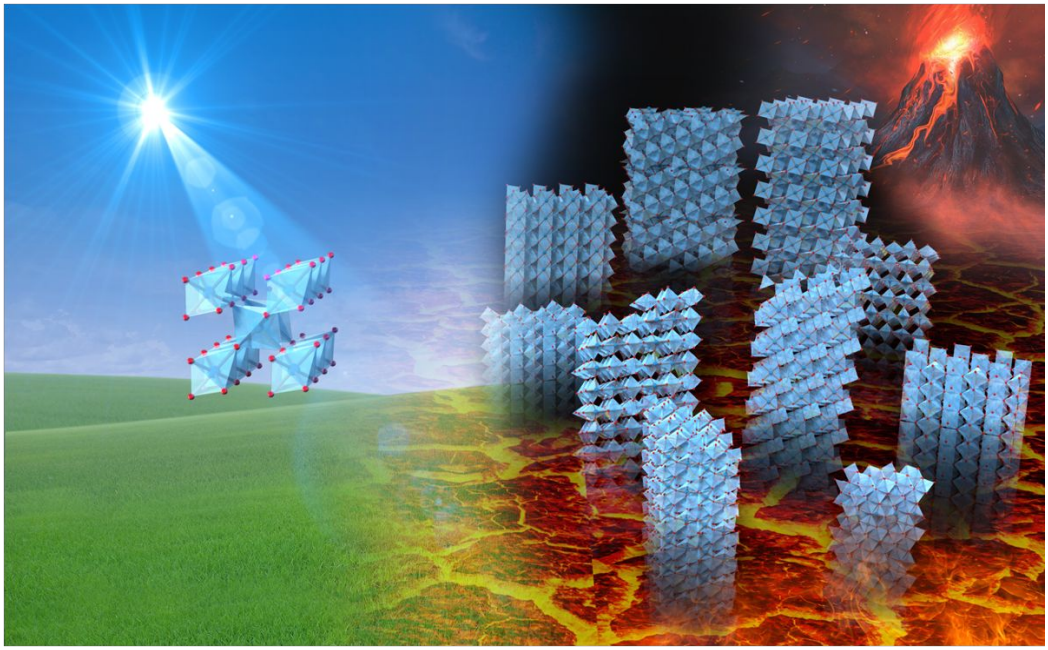

Figure 1. Comparing the complexities of surface structures with a bulk structure inspired by the famous quote: “God made the bulk; surfaces were invented by the devil”.

2. Simple binary oxide surfaces[47]

Metal oxides play significant roles in heterogeneous catalysis, which is largely governed by surface point defects, such as O vacancies. For instance, the MvK mechanism, in which O vacancy sites on a metal oxide catalyst surface act as reaction sites, is a frequently encountered catalysis process.[13,14] In addition, metal–support interactions (MSIs) have been ascribed to oxide reducibility as measured by the surface oxygen vacancy formation energy (E_{Ovac}).[48]

As part of our work,[47] we calculated E_{Ovac} values for insulating and semiconducting oxides, with the most stable surface for each compound/structure used in this study, as shown in **Figure 2**. Both (111) and $(11\bar{1})$ surfaces were considered for the Baddeleyite structure because their surface energies (E_{surf}) are almost the same. The obtained E_{Ovac} values were correlated with other readily available physical properties, such as the bulk formation energy per atom (E_{form}), E_{surf}, the Kohn–Sham BG, electron affinity (EA; negative of the conduction band minimum (CBM) with respect to the vacuum level), ionization potential (IP; negative of the valence band maximum (VBM) with respect to the vacuum level), and work function (WF; defined as the average of IP and EA for insulating and semiconducting materials). In addition to these computationally derived properties, electronegativity (EN) was calculated as the geometrical mean of the Pauling ENs of the atoms in the system according to Sanderson's definition.[49]

Linear correlations between E_{Ovac} and descriptors mentioned above were examined (**Figure 3**). BG was found to be the best descriptor (R^2 = 0.74) among those explored; a large BG results in a large E_{Ovac} (O vacancies are difficult to form), which is physically reasonable because O is formally an anion with excess electrons in such a compound; its removal generally forces excess electrons to be transferred somewhere above the VBM, with the most obvious place being the CBM. Electrons enter defect states after O removal, and these states can either be in the valence band, the mid-gap, or the conduction band. Excess electrons are expected to be transferred to the CBM in many cases, which modulates the stabilities of the remaining excess electrons through the formation of O vacancies, which explains why the BG (i.e., the difference between the CBM and VBM) correlates well with the E_{Ovac} value. Similar trends were observed in computational investigations of bulk models.[50–54] Understanding the correlations among descriptors also provides guidelines for selecting combinations of descriptors when constructing ML models and obtaining chemical/physical insights from the models. For example, the correlation between EA and WF is high (0.94), indicating that using these quantities together can be redundant for ML studies.

The BG is not the single driver of E_{Ovac}; otherwise, all metallic compounds with a zero BG would have the same E_{Ovac}. In fact, our density-of-states-based (DOS-based) defect state analysis suggests that the BG cannot be a single descriptor in light of the observed defect-state-position diversity.[47] In short, reality is more complex. Some correlation with E_{form} is expected because the removal of O requires cation−O bond cleavage; therefore, E_{form} must reflect bond strength. In fact, the E_{form} of the metal oxide was found to be the second most important descriptor (R^2 = 0.55).

The subsequent adsorption of molecular CO, CO_2, O_2, NO, and H_2 on O-deficient surfaces

was also investigated (**Figure 4**), which is of significant importance because surface defect sites are often involved in the adsorption process, a fundamental step in a surface-catalyzed reaction. Note that only systems with negative adsorption energies (i.e., for which adsorption is likely to occur) are plotted here. E_{Ovac} was found to linearly correlate with adsorption energy for each molecular species considered. These results show that E_{Ovac} is a general descriptor for the adsorption of a molecule on a defective surface, which is an important catalysis step on an oxide surface. The results potentially serve as a practical guide for the design of advanced catalysts and provide insight into the chemical and physical principles that govern heterogeneous catalysis processes.

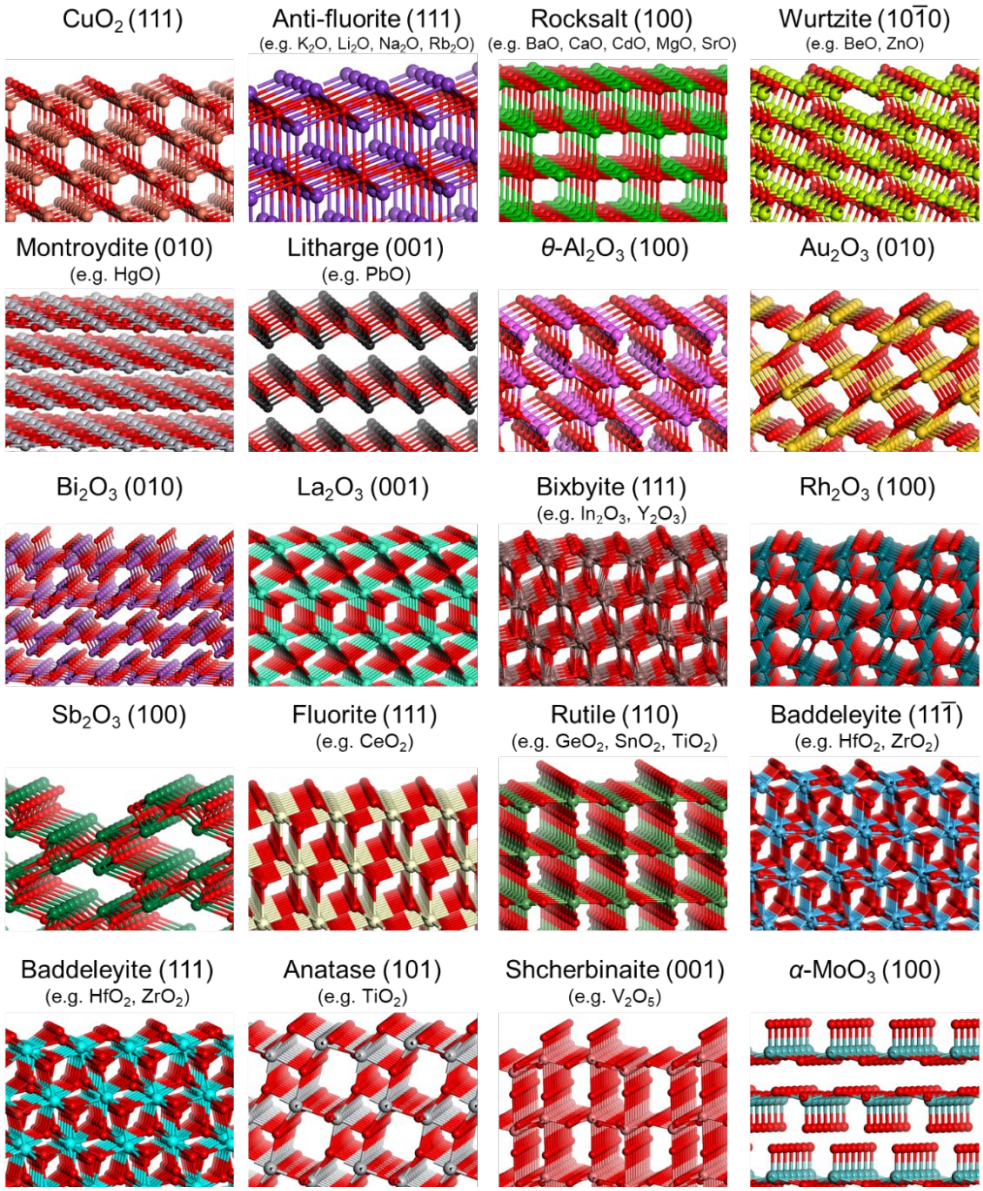

Figure 2. Representative surfaces of some simple binary oxides investigated.

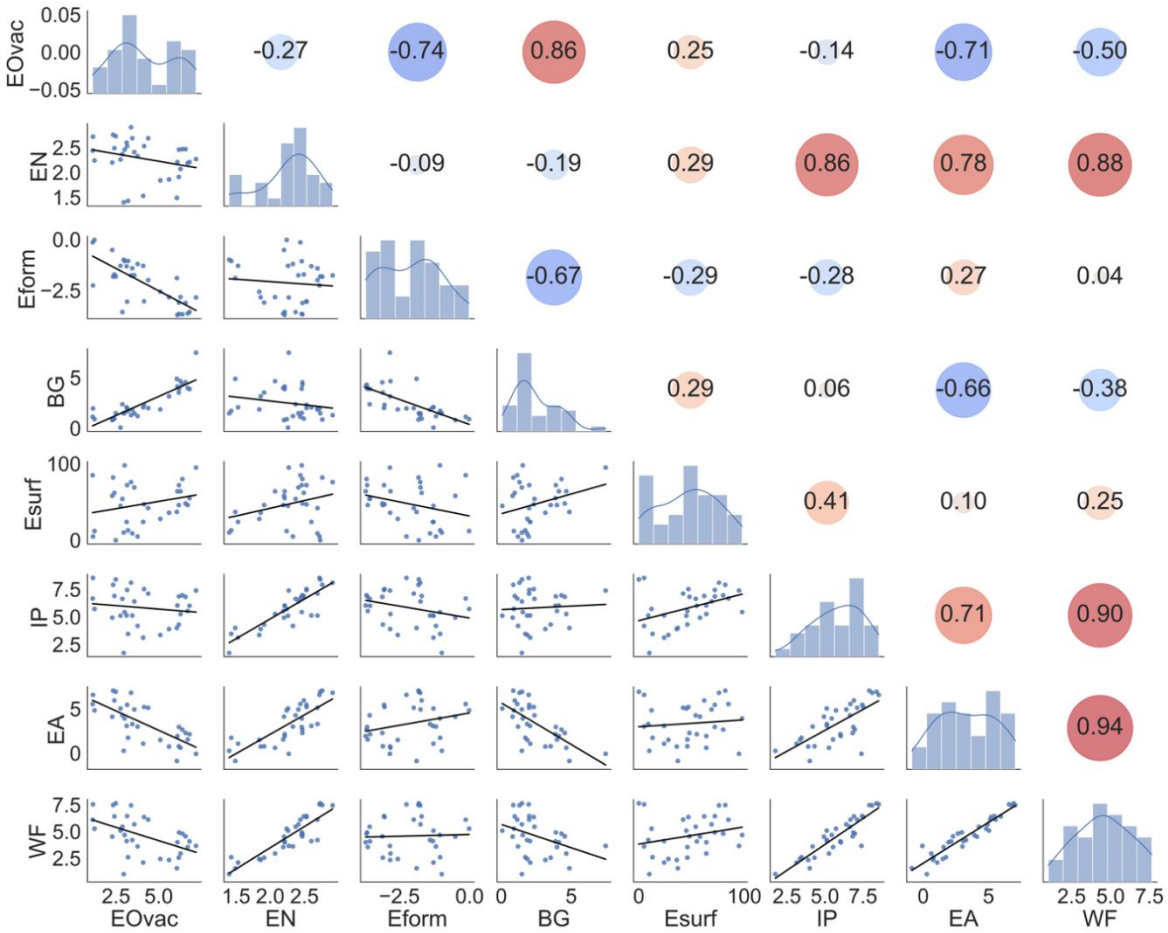

Figure 3. Correlations between E_{Ovac} and other physicochemical properties of oxide surfaces. The numbers are correlation coefficients (R).

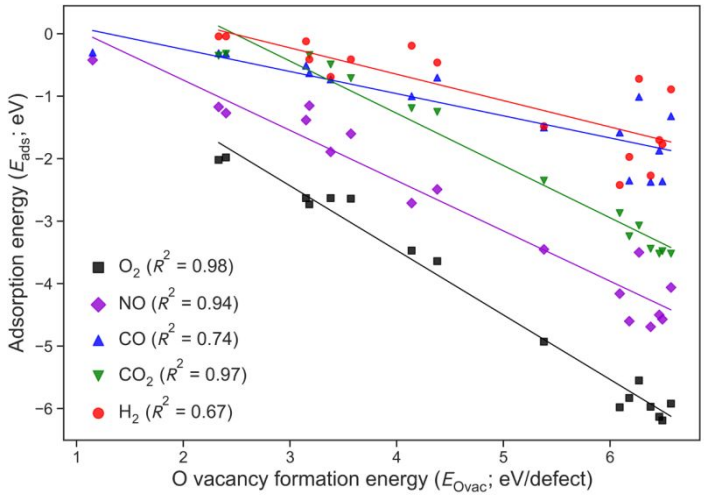

Figure 4. Adsorption energies for CO, CO_2, O_2, NO, and H_2 on O-removed surfaces as functions of the E_{Ovac} value of the binary oxide surface. Only the cases where the E_{ads} values are negative (adsorption is likely to occur) are shown. The E_{ads} of CO and NO were calculated for C-down and N-down adsorption on O-vacancy sites, respectively, while the E_{ads} of CO_2 and H_2 were calculated for both molecular and dissociative adsorption, and the stable structure was adopted.

3. Mixed oxide surfaces[55]

Mixed oxides are among the most widely used materials for industrial catalytic processes. They exhibit unique properties that are ascribable to their diverse structures for which characteristics can be tailored by choosing constituent elements.[56,57] Among various mixed oxide materials, AB_2X_4 spinels are regarded as one of the most important class of crystalline compound in catalysis.[56] Here A is a divalent cation, B is a trivalent cation, and X is a divalent anion in the stoichiometric formula of a (normal) spinel compound; X is O for a spinel oxide. The A and B cations also occupy two different sites, namely octahedral (O_h) and tetrahedral (T_d) sites. Spinel oxide catalysts have been used to realize various CO_2 hydrogenation reactions, with Zn-based spinel oxides proving to be particularly effective. For instance, a catalytic system consisting of $ZnGa_2O_4$ and SAPO-34 has been used to convert CO_2 into lower olefins.[58] In addition, bifunctional catalytic systems comprising $ZnCr_2O_4$ or $ZnFe_2O_4$ and a zeolite were found to be effective for the direct conversion of CO_2 into aromatic compounds.[59,60] Zn-based spinel oxides are responsible for CO_2 activation in all of these systems, with their O vacancies playing significant roles in the efficient progression of each reaction. Understanding the nature of the O vacancies of Zn-based spinel oxides and subsequent CO_2 activation on these vacancies is expected to lead to the rational design of effective catalysts for CO_2 transformation reactions.

With this background in mind, we calculated the E_{Ovac} values and electronic structures for the (100), (110), and (111) surfaces of $ZnAl_2O_4$, $ZnGa_2O_4$, $ZnIn_2O_4$, ZnV_2O_4, $ZnCr_2O_4$, $ZnMn_2O_4$, $ZnFe_2O_4$, and $ZnCo_2O_4$, which are normal zinc-based spinel oxides, as shown in **Figure 5**;[55] the (100) surface was found to be most stable in each case. With the exception of $ZnCo_2O_4$, the smallest E_{Ovac} was found to be largest on the (100) surface, and the values for the (100) and (110) surfaces were found to correlate well with the E_{form} value for each spinel.

ML was also used to statistically analyze and predict E_{Ovac} values for all surface O sites of ZnM_2O_4 and to identify factors that are predictively important, using the descriptors discussed above, namely E_{form}, IP, EA, BG, and the geometric descriptors. The type of surface orientation was also implemented using a one-hot encoding method. Well-performing ML methods were evaluated with a set of six widely used ML methods, namely the least absolute shrinkage and selection operator (LASSO) and ridge regression linear methods, support vector regression (SVR) and Gaussian process regression (GPR), as kernel methods, and random forest regression (RFR) and extra tree regression (ETR), as tree ensemble methods. Monte Carlo cross-validation with 100 random leave-10%-out trials was performed to obtain the average root-mean-square error (RMSE) and to evaluate the predictive capability of each ML model. **Figure 6(A)** demonstrates that the six ML methods tested in this study were able to predict E_{Ovac} to within an RMSE of 0.49–0.77 eV/defect. Tree ensemble methods performed relatively well, with ETR determined to be the most predictively accurate. R^2 was also determined to be 0.82 for the ML model based on ETR, which demonstrates that E_{Ovac} can be predicted using a dataset with only 106 data points and readily available descriptors. Accuracy is expected to be improved once more data are obtained in the future. As a side note: we are arguably

still observing overfitting to the training data and non-negligible gaps between training and test errors for the best-performing model based on ETR. This observation has recently been discussed in terms of "benign overfitting" in modern ML models and remains an involved problem in the community.[61–63] In principle, ETR works as a pseudo piecewise-linear interpolation, and given a small number of data points, interpolating noisy training data can be more informative and give better prediction rather than also trying to separate noise out in such underspecified cases with small samples. We confirmed that ETR with bootstrapping did not improve prediction performance.

With the best ML method (ETR) in hand, the SHapley Additive exPlanations (SHAP) technique was then used to identify and prioritize descriptors, as shown in **Figure 6(B)**; i.e., the contribution of a given input feature to the target (E_{Ovac}) response was identified.[64,65] The most important descriptor was found to be E_{form}, followed by the type of surface orientation, IP, and coordination number. As expected, E_{form} is a significantly important descriptor, with the Surface(111) descriptor contributing highly because, unlike the other two surfaces, E_{Ovac} and E_{form} correlate poorly for the (111) surface. This analysis also revealed that E_{Ovac} (SHAP value) tended to be high for low E_{form} (feature value), which indicates that not only is bulk property information necessary, but information on the local structures of surface O sites is also necessary. In addition, both geometrical and electronic properties were identified to be important for predicting E_{Ovac}. Breakdown of SHAP values as waterfall plots for two representative surfaces ($ZnAl_2O_4$ (110) and $ZnCo_2O_4$ (111)) are also shown in **Figure 6(C,D)**. For example, in $ZnAl_2O4$ (110), it can be seen that the high E_{Ovac} value is mainly due to the large absolute value of E_{form} and the fact that the surface orientation is not (111). On the other hand, for $ZnCo_2O_4$ (111), the relatively small absolute value of E_{form} and the unstable (111) surface contribute to lowering the E_{Ovac} value. These additional analysis reveals which descriptors are responsible for increases and decreases from the dataset average value (3.13) relative to the predicted value.

Figure 5. E_{Ovac} values for all surface O sites and all ZnM_2O_4 surfaces as functions of E_{form}.

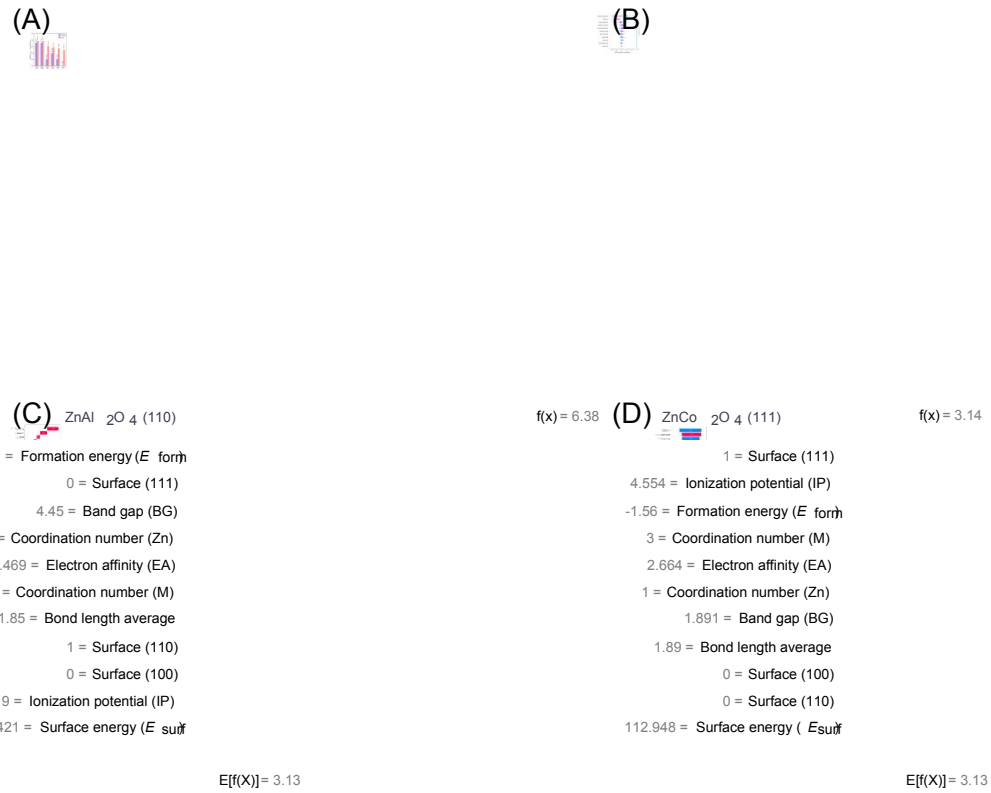

Figure 6. (A) Average RMSEs for predicting E_{Ovac} for all ZnM_2O_4 surface O sites from 100 random leave-10%-out trials using various ML methods. (B) SHAP values of the descriptors used to predict E_{Ovac} using ETR. SHAP values of individual factors are plotted as dots (blue corresponds to low features, red to high features). Here, features are ordered in descending order according to the sum of their absolute SHAP values. Breakdown of SHAP values as waterfall plots for (C) $ZnAl_2O_4$(110) and (D) $ZnCo_2O_4$(111) is provided to determine which feature values are responsible for increases and decreases from the base value (dataset average: E[f(X)]) of 3.13 relative to the predicted value. Positive and negative contributions of each feature (SHAP values: f(x)) are shown in red and blue, respectively.

4. High-index oxide surfaces[66]

Oxides are expected to exhibit high catalytic reactivities at high-index surfaces and at surface defects, such as corners and step edges, because cations and anions in these environments exist in more unfavorable coordination environments and have lower coordination numbers than atoms on smooth faces or in the bulk. Computational studies on irregular sites are leading experimental ones owing to difficulties associated with the latter. An actual oxide particle can have many exposed orientations; hence, the development of an algorithm that can rapidly model diverse surfaces and considers surface reconstruction is expected to be very helpful because attempts to experimentally synthesize high-index surfaces and unstable surface sites, which can be handled computationally, fail because stable surfaces become reconstructed.

We developed a workflow that efficiently produces a set of accessible terminations by removing those that are metastable against macroscopic facet formation, and compared the cleaved surfaces with surfaces suggested by a genetic algorithm (GA) for promising orientations using 34 orientations of β-Ga_2O_3 and θ-Al_2O_3.[66] Seven and six terminations, which are considered to be experimentally accessible, were located for β-Ga_2O_3 and θ-Al_2O_3, respectively, for which the highest E_{surf} was roughly twice that of the lowest. The lowest E_{Ovac} among the accessible surfaces were found to be 3.04 and 5.46 eV for the (101) and $(20\bar{1})$ terminations of β-Ga_2O_3 and θ-Al_2O_3, respectively, which are 1.32 and 1.11 eV, respectively, lower than those of the most stable surfaces.

Correlations between minimum E_{Ovac} values and a number of descriptors were determined for β-Ga_2O_3 and θ-Al_2O_3, thereby providing insight into the formation of O vacancies on exotic surfaces. As mentioned above, the E_{Ovac} values of stable surfaces are strongly related to bulk BG and E_{form}, while the bulk O vacancy formation energy correlates with the BG, E_{form}, mid-gap energy relative to the O 2*p* band center, and atomic electronegativities.[52,67] However, these descriptors cannot be used when investigating different terminations of the same crystal. Three descriptors were examined, namely, the E_{surf}, IP, and BG of each surface slab model. Plots of minimum E_{Ovac} as functions of E_{surf} for the various surfaces, which showed the best R^2 among the three descriptors for both compounds, are shown in **Figure 7**. E_{Ovac} decreases with increasing E_{surf}, which is natural because less stable surfaces may have O in less favorable environments that can be removed with less energy. In addition, the E_{Ovac} values on accessible surfaces show good correlations with local coordination environment descriptors, which suggests that exploiting surface O in an unfavorable environment in an experimentally accessible termination enhances O-vacancy-related catalyst performance even in materials that are unreactive on their most stable surfaces.

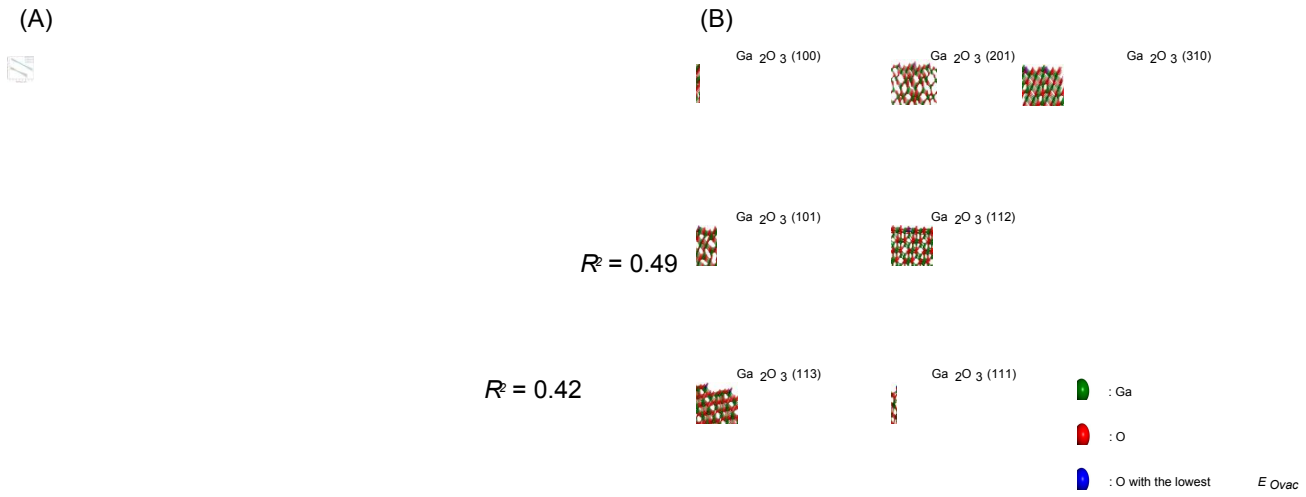

Figure 7. (A) E_{Ovac} vs. E_{surf} for β-Ga_2O_3 and θ-Al_2O_3. R^2 values for the linear fits of all terminations, only accessible terminations, and only inaccessible terminations are also given, respectively. (B) Accessible terminations of β-Ga_2O_3. Green, red, and blue balls indicate Ga, O, and O sites with the lowest E_{Ovac}, respectively.

5. Carbides, nitrides, sulfides, and hydrides[68]

Metals and metal oxides play central roles in heterogeneous catalysis.[69] However, the use of less-explored classes of compound as catalysts is always crucial when exploring new processes,[70] with metal nitrides, carbides, sulfides, and hydrides among such materials.[71,72] While these compounds are not new, there is growing interest in their catalytic properties and potential applications that include thermal, photo-, and electro-catalysis.[73,74] For instance, nitrides and carbides are known to play roles in a number of valuable catalytic processes, such as NH_3 synthesis,[75] Fischer–Tropsch synthesis,[76] and hydroprocessing.[77] Sulfides have also been extensively used in the petroleum industry.[78,79] Although hydrides have been less explored in heterogeneous catalysis, these materials, including surface hydrides as well as hydride-containing mixed-anion compounds, have received much attention recently for use in a variety of catalytic processes, including NH_3 synthesis and CO_2 hydrogenation, where surface H species play important roles.[80–82]

The catalytic reaction mechanisms of the aforementioned materials are of significant interest. In particular, the MvK mechanism, where surface anion vacancies serve as active centers, is often considered for this class of material.[83] Recently, Zeinalipour-Yazdi et al. investigated the mechanism of the NH_3 synthesis reaction over Co_3Mo_3N using DFT calculations and found that this reaction can proceed through a N-based MvK mechanism.[84] In addition, several studies have reported that Fischer–Tropsch syntheses over Fe carbides proceed by a MvK mechanism involving the liberation of carbon from the carbide surface and the dissociative adsorption of CO, which recovers the carbide surface by filling carbon vacancies.[85–87] Although such work greatly contributes to the body of knowledge on the catalysis of non-oxide-based materials, our present understanding of their catalytic roles and surface properties remains insufficient.

In our study,[68] surface properties, such as work function (WF), were calculated for binary compounds in which the cation is a group 3, 4, or 5 element (i.e., Sc, Y, La, Ti, Zr, Hf, V, Nb, or Ta) and the anion is either H, C, N, O, or S. **Figure 8** shows the WF values of representative surfaces of the considered compounds. With the exception of YN, which has a very small bandgap (0.07 eV), these compounds are all metallic, with WFs smaller than that of Ag (4.56 eV) (with the exception of TiC, whose WF is close to 4.61 eV). In contrast, the oxides and sulfides exhibit large WF ranges of 1.97–8.33 eV and 2.28–6.02 eV, respectively. Many oxides and sulfides feature BGs; hence, values of IP and EA that exclude the explicit effects of in-gap surface states are also shown. The oxides and sulfides exhibited lower WFs when their cations were reduced.

Many low-WF systems share the same crystal structure; therefore, the relationship between the cation and the E_{vac} value of the surface anion was investigated for the fluorite (111) surfaces of hydrides and the rocksalt (100) surfaces of nitrides and group 4 and 5 carbides. Some of the investigated compounds were hypothetical, but were included to observe trends over a wider range of elements. In addition, identifying correlations between the surface-anion vacancy-formation energies and other physicochemical quantities enables E_{vac} to be rationalized and predicted, which is beneficial when screening materials for specific applications in a significantly computationally cost-

effective manner. With the aim of identifying general versatile relations, correlations between E_{vac} and the physicochemical properties of various hydrides, carbides, and nitrides, as well as the elemental properties of the cations and anions in these compounds, are shown in **Figure 9**. For the properties of the compounds themselves, E_{form} and WF provide relatively high correlation coefficients, although the M–X_{vac} length and the bulk density, correlate poorly with E_{vac}. These results highlight the importance of both structural and electronic properties when developing an understanding of E_{vac}, which is consistent with the aforementioned discussion on oxide surfaces. Regarding elemental properties, EA and cation electronegativity were found to correlate well with E_{vac} (high R). Note that BG, which serves as a good E_{Ovac} descriptor for many oxide surfaces (see section 2), was not considered as a descriptor here because all of the hydrides, carbides, and nitrides considered have zero BGs.

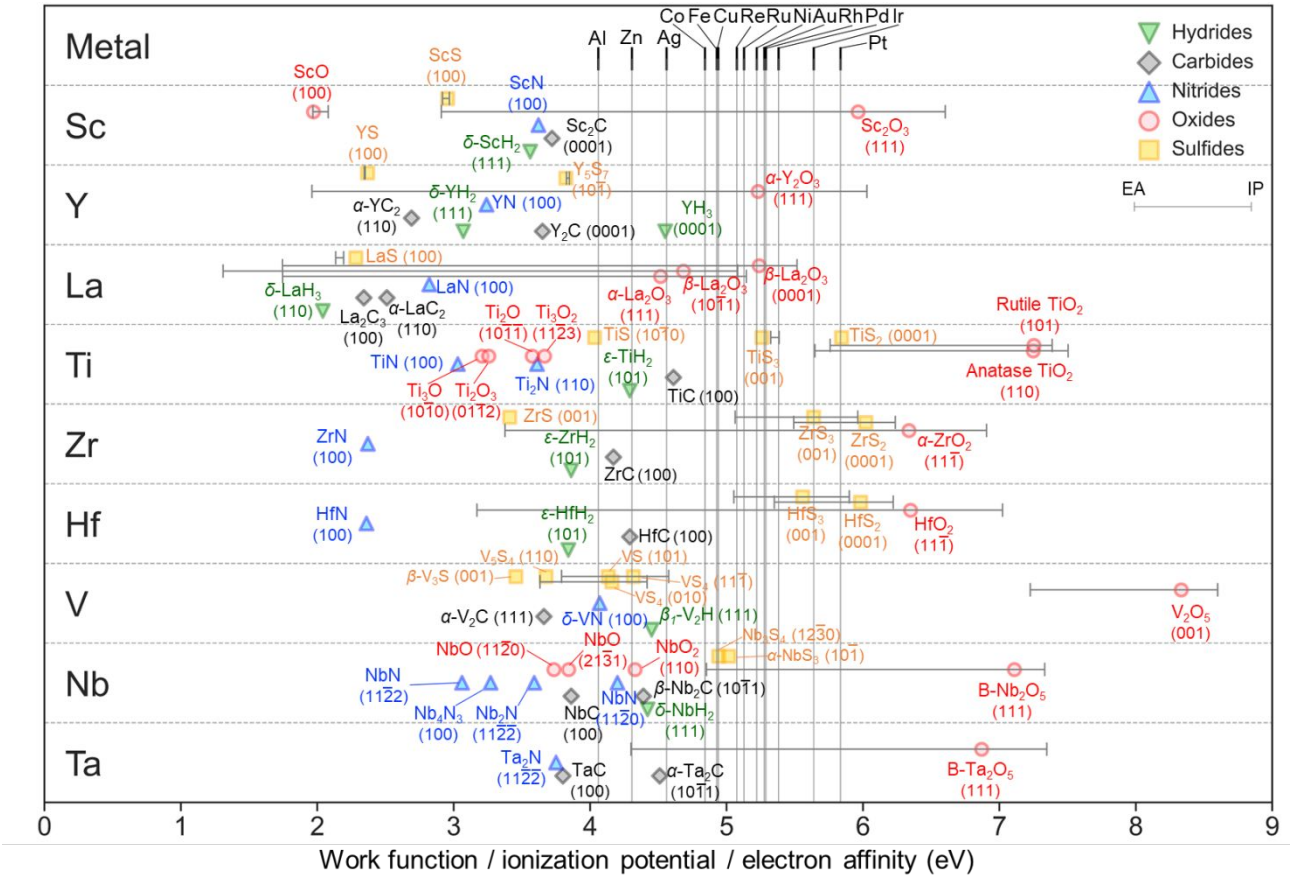

Figure 8. WFs of representative hydride, carbide, and nitride compound surfaces, as well as IPs and EAs based on bulk definitions (bars). The WFs of elemental metals (crosses) are also shown.

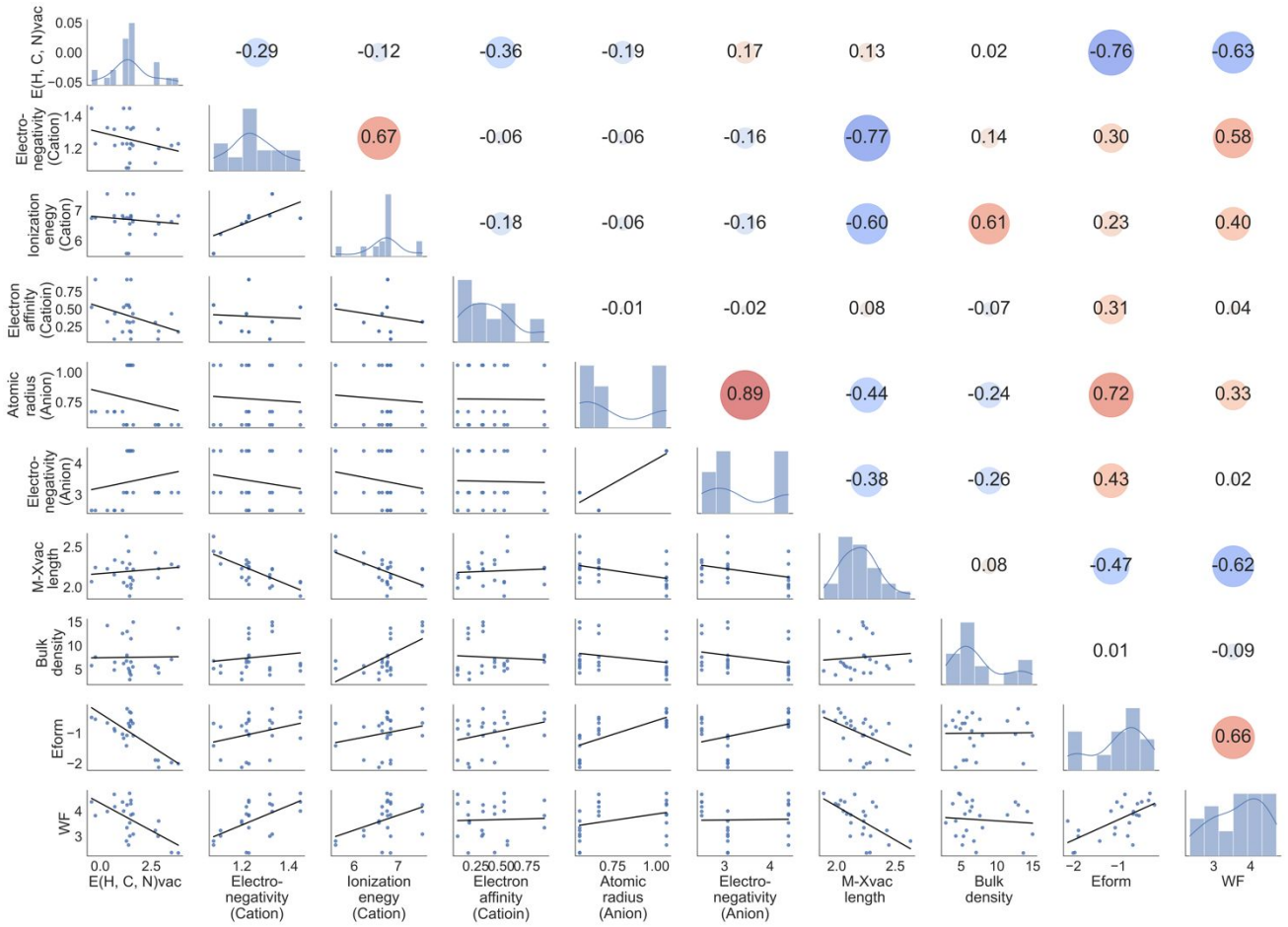

Figure 9. Correlation map of E_{vac}, physicochemical properties of hydrides, carbides, and nitrides, and the properties of elemental cations and anions associated with these compounds (M and X, respectively). The physicochemical properties of the hydrides, carbides, and nitrides include WF, E_{form}, bulk density, and length of the M–X bond (M-X_{vac} length), where X is the atomic anion to be removed. Here, E_{vac}, WF, E_{form}, and M-X_{vac} length were obtained using DFT calculations while elemental properties of the cations and anions were obtained from the CRC handbook. The numbers are correlation coefficients (R).

6. Metal/oxide perimeter sites[88]

The interaction between a metal nanoparticle and its oxide support has been extensively discussed in the heterogeneous catalysis field.[89–93] The supported metal nanoparticle and the support itself affect each other in a manner that creates unique surface properties and electronic structures.[94] Sites located in the immediate vicinity of the metal/oxide interface, referred to as "perimeter sites", are often considered to be the catalytically active sites.[95,96] For instance, supported noble metal nanoparticles can promote the formation of surface O vacancies in reducible metal oxide supports at perimeter sites, which serve as active redox centers for various reactions through the MvK mechanism.[97,98] Despite its importance in the broad field of heterogeneous catalysis, the nature of the interaction between a metal nanoparticle and its metal oxide support, and its effect on O-vacancy formation, have not been extensively investigated due to the complexity of the system; consequently, it remains a key heterogeneous catalysis research area.[11] Computational approaches that address this issue[99–102] in a systematic fashion and in a manner that investigates the underlying physics/chemistry are necessary, as accessing such systems experimentally is difficult due to their complex nature.

Group 13 metal oxides, including In_2O_3, Ga_2O_3, and Al_2O_3, show unique properties and serve as excellent catalysts and supports for various valuable chemical transformations.[103,104] In particular, much attention has been paid to In_2O_3 recently. In_2O_3 was found to promote the hydrogenation of CO_2 to methanol, with its surface oxygen vacancies playing significant roles in the efficient progression of the reaction.[105–107] Performance can be further improved by combining this material with a second component, such as Pd,[108,109] Co,[110] or Ni.[111] Interactions between In_2O_3 and the second active component are key to creating more oxygen vacancies that are responsible for adsorbing and activating reactants.

Our study considered the adsorption of metal nanoparticles on an In_2O_3 slab with a (111) surface,[88] and the metal element, M, was selected from among Cu, Ag, Au, Pd, Pt, Ir, and Re. The M/In_2O_3 system was modeled as a semi-infinite M nanorod supported on In_2O_3 (111); similar models have been employed for investigating metal/oxide sites at perimeters and interfaces (**Figure 10A**).[112,113] One major objective of this study was to systematically analyze differences under the same computational conditions, thereby enabling direct comparisons over seven elements M. Specifically the relationship between the E_{Ovac} value of the In_2O_3 (111) surface and the adsorbed metal nanorod was investigated.

Although the change in E_{Ovac} upon nanorod adsorption depends on the O site and the type of element M, it tends to be lowered by adsorption (O vacancies are likely to form), especially for Pt, Ir, and Pd. In addition, such decreases in E_{Ovac} were mainly observed at O sites near the nanorod. The minimum E_{Ovac} value for each system is primarily discussed here, as our main objective was directed toward investigating the effect of the type of metal M. The minimum E_{Ovac} values were found to depend on M (Re > Ag > Cu > Au > Pt > Ir > Pd) and to show a fair correlation with WF (R^2 = 0.55), as shown in **Figure 10B**. In addition, minimum E_{Ovac} was found to correlate better with degrees of electron transfer (Bader charge) from support to nanorods upon removal of O giving a minimum E_{Ovac}

(R^2 = 0.83, see **Figure 10C**). Here, we discuss the reason why M can be grouped into three sets, namely, {Ag, Cu, Re}, {Au}, and {Ir, Pd, Pt}, in terms of the relationship between E_{Ovac} and the level of electron transfer to the M. **Figure 10D** shows electronic DOSs of the In_2O_3 bulk, the In_2O_3 slab without O vacancies, the In_2O_3 slab with one O vacancy on each side that minimizes E_{Ovac}, and the WF of M. Cleavage to form a surface results in surface-induced states just above the bulk VBM, while the removal of O results in occupied defect states higher than these surface-induced states. The E_F values in O-desorbed In_2O_3 are higher than the Pt, Ir, and Pd WFs, lower than the Re, Cu, and Ag WFs, and almost the same as the Au WF, which suggests that charge transfer from defect states to the nanorod reduces the Pt, Ir, and Pd energies; therefore, these M atoms act as electron scavengers that lower E_{Ovac} by inducing interactions between M and In_2O_3. In contrast, Re, Cu, and Ag cannot act as strong electron scavengers, while Au can act as an electron scavenger to some extent. To further understand the charge transfer from defect states to nanorods, an analysis of the charge density distribution was conducted. **Figure 10E** shows charge transfer when M is Pd, and the site of O removal was taken very close to the Pd nanorod. The charge transfer in the case of M = Cu, Ag, Au, and the case where O atoms far away from the nanorods were removed has been investigated in our previous reports.[88] Charge transfer from the O-defect sites near the Pd nanorods (blue spheres, highlighted by blue inverted lines) onto the Pd nanorods can be observed. Similar results were obtained for Ag and Au, and the amount of charge transfer from the support to the nanorod qualitatively becomes larger in the order Ag, Au, and Pd, which means that more charge is transferred from the support site to the metal nanorod when the WF of the metal is larger. This result indicates that E_{Ovac} can be controlled by the combination of catalyst supports and supported metals. These observations are consistent with previous theoretical studies on relevant metal/oxide systems. Puigdollers and Pacchioni demonstrated that excess electrons are transferred to Au when O is removed from a ZrO_2 support with a Au nanoparticle adsorbed on its surface when the vacancy site is close to the nanoparticle.[114] E_{Ovac} was lowered by up to 2.2 eV in Au-nanorod-adsorbed anatase TiO_2 when the vacancy site was close to a Au nanorod.[115] Bazhenov et al. observed a steep drop in E_{Ovac} at O sites near the nanoparticle in Rh-nanoparticle-adsorbed ZrO_2, which was ascribed to the accommodation of electrons by Rh where E_{Ovac} decreases.[116] It is important to note that geometrical relaxation had less of an effect in our system, as the M atoms barely moved upon removal of surface O, which enabled precise analysis of the effect of charge transfer alone when analyzing differences in minimum E_{Ovac} across various elements M. These observations assist in the selection of nanoparticles that activate the surface sites of the support.

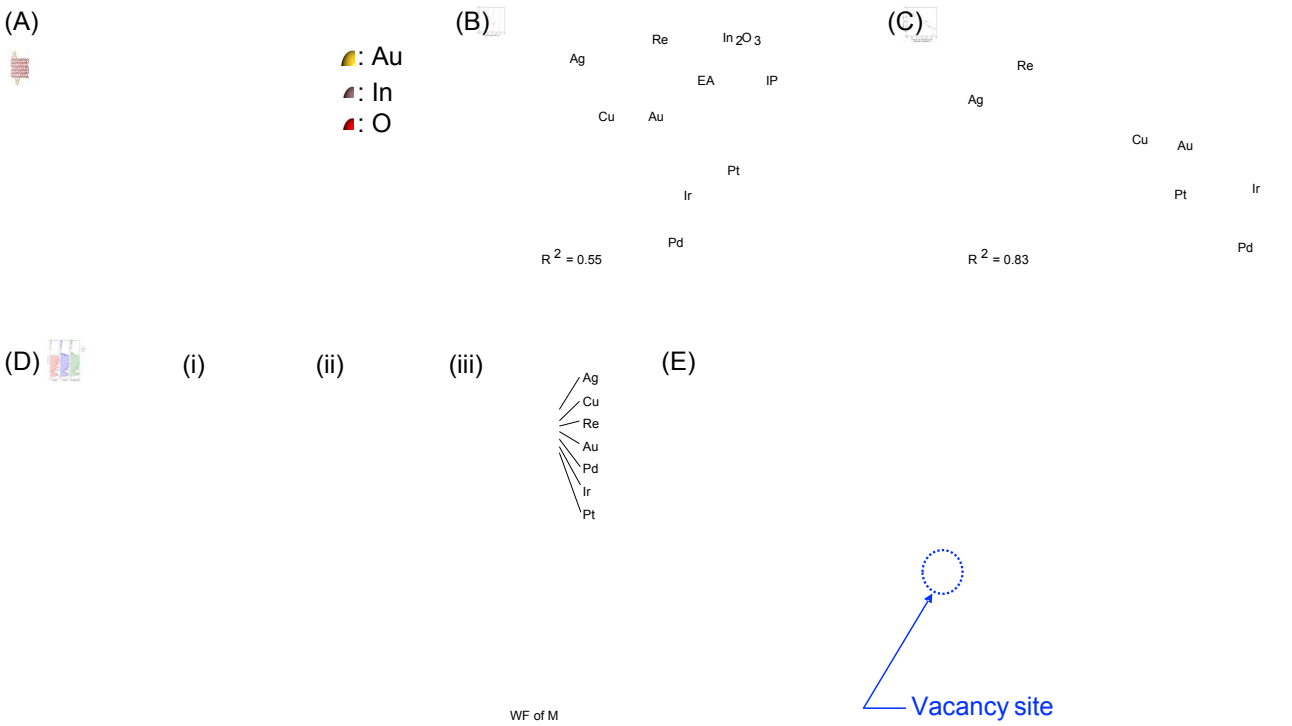

Figure 10. (A) Representative model for the adsorption of M nanorods on In_2O_3. Red and brown balls indicate O and In, respectively, while gold-colored balls represent M (Au in this case). Plots of minimum E_{Ovac} as functions of (B) the WF of the M slab with EA and IP of an In_2O_3 (111) slab and (C) the change in nanorod Bader charge upon O desorption. (D) Site-projected DOSs of (i) the In_2O_3 bulk, (ii) the In_2O_3 (111) slab without O vacancies, (iii) In_2O_3 (111) slab with one O vacancy on each side that minimizes E_{Ovac}, and WF of M. The bulk and slab DOSs without vacancies are aligned using the average local potential at atomic sites, and the slab DOSs with and without O vacancies and the metal WF are aligned at the vacuum level. (E) Charge-density transfer from the support to the Pd nanorod with O vacancy formation. The charge density of the isosurface is 0.1 (elementary charge / $Å^3$).

7. Conclusions and future outlook

Discovering new catalysts is a formidable challenge; consequently, many of the advances in the catalysis field have arisen through trial-and-error investigations, which are often very resource-intensive and intellectually frustrating. Establishing effective and accurate catalyst design guidelines by providing a fundamental understanding of catalytic materials and processes will accelerate the further development of high-performance catalysts. In this perspective, we summarize a series of studies aimed at understanding and controlling the formation of surface anion vacancies, which can serve as active sites for a number of catalysis applications. In addition to obtaining E_{vac} values as important descriptors of catalytic performance, we examined correlations between surface anion E_{vac} values and the physicochemical properties of compounds/surfaces together with those of support metals by deconvoluting observed trends into electronic structures. Despite limitations in computational accuracy and the existing diversity of metal-oxide surfaces, our efforts provide guidance for the design of solid catalysts.

Many challenges currently remain, ranging from fundamental chemistry/physics to computational issues and the design of materials with tailored properties. The systematic rationalization of anion vacancies through experimental observations of a large number of surface systems remains unexplored and unrealistic because sophisticated techniques that are both time- and cost-intensive are required, and evaluating E_{vac} is not always possible even when state-of-the-art techniques are used. In terms of computational challenges, the inability to match defect calculations performed using various incarnations of electronic structure theory is a major problem.[117] The need to carry out post-DFT corrections reduces the transferability and predictive power of these methods. Problems related to surface termination and structure are ubiquitous. The development of automated methods for calculating defects and subjecting the results to ML can potentially overcome these limitations.[118–120] On the other hand, finding descriptors that are highly correlated with the formation of anion vacancies on various solid surfaces with different geometries and electronic properties is an expected role of the ML approach, but we still need to improve datasets for this purpose. Finally, the ability to design and synthesize new catalyst materials with specific properties by manipulating surface imperfections remains a great challenge in catalysis science.

Acknowledgments

The preparation of this perspective and the studies carried out by the authors were supported by JST-CREST Project JPMJCR17J3 and KAKENHI (Grant No. 20H02775, 20KK0111, 20F20345, and 21K18185) from the Japan Society for the Promotion of Science (JSPS). DFT calculations were performed on supercomputers at RIIT (Kyushu Univ.) and ACCMS (Kyoto Univ.).

References

1 G. Pacchioni, *ChemPhysChem*, 2003, **4**, 1041–1047.

2 M. V. Ganduglia-Pirovano, A. Hofmann and J. Sauer, *Surf. Sci. Rep.*, 2007, **62**, 219–270.

3 F. Oba, M. Choi, A. Togo and I. Tanaka, *Sci. Technol. Adv. Mater.*, 2011, **12**, 034302.

4 N. Daelman, F. S. Hegner, M. Rellán-Piñeiro, M. Capdevila-Cortada, R. García-Muelas and N. López, *J. Chem. Phys.*, 2020, **152**, 050901.

5 R. Rousseau, V. A. Glezakou and A. Selloni, *Nat. Rev. Mater.*, 2020, **5**, 460–475.

6 A. A. Emery, J. E. Saal, S. Kirklin, V. I. Hegde and C. Wolverton, *Chem. Mater.*, 2016, **28**, 5621–5634.

7 C. Linderälv, A. Lindman and P. Erhart, *J. Phys. Chem. Lett.*, 2018, **9**, 222–228.

8 J. S. Park, S. Kim, Z. Xie and A. Walsh, *Nat. Rev. Mater.*, 2018, **3**, 194–210.

9 C. Freysoldt, B. Grabowski, T. Hickel, J. Neugebauer, G. Kresse, A. Janotti and C. G. Van De Walle, *Rev. Mod. Phys.*, 2014, **86**, 253–305.

10 X. Yu, T. J. Marks and A. Facchetti, *Nat. Mater.*, 2016, **15**, 383–396.

11 A. R. Puigdollers, P. Schlexer, S. Tosoni and G. Pacchioni, *ACS Catal.*, 2017, **7**, 6493–6513.

12 J. Jia, C. Qian, Y. Dong, Y. F. Li, H. Wang, M. Ghoussoub, K. T. Butler, A. Walsh and G. A. Ozin, *Chem. Soc. Rev.*, 2017, **46**, 4631–4644.

13 K. Chen, A. Khodakov, J. Yang, A. T. Bell and E. Iglesia, *J. Catal.*, 1999, **186**, 325–333.

14 D. Widmann and R. J. Behm, *Acc. Chem. Res.*, 2014, **47**, 740–749.

15 G. Kumar, S. L. J. Lau, M. D. Krcha and M. J. Janik, *ACS Catal.*, 2016, **6**, 1812–1821.

16 K. Werner, X. Weng, F. Calaza, M. Sterrer, T. Kropp, J. Paier, J. Sauer, M. Wilde, K. Fukutani, S. Shaikhutdinov and H. J. Freund, *J. Am. Chem. Soc.*, 2017, **139**, 17608–17616.

17 C. Yang, X. Yu, S. Heißler, P. G. Weidler, A. Nefedov, Y. Wang, C. Wöll, T. Kropp, J. Paier and J. Sauer, *Angew. Chemie - Int. Ed.*, 2017, **56**, 16399–16404.

18 S. Agarwal, X. Zhu, E. J. M. Hensen, L. Lefferts and B. L. Mojet, *J. Phys. Chem. C*, 2014, **118**, 4131–4142.

19 Z. Zhang, O. Bondarchuk, J. M. White, B. D. Kay and Z. Dohnálek, *J. Am. Chem. Soc.*, 2006, **128**, 4198–4199.

20 X. Tong, L. Benz, S. Chrétien, H. Metiu, M. T. Bowers and S. K. Buratto, *J. Phys. Chem. C*, 2010, **114**, 3987–3990.

21 G. Pacchioni and H. Freund, *Chem. Rev.*, 2013, **113**, 4035–4072.

22 M. Setvín, M. Wagner, M. Schmid, G. S. Parkinson and U. Diebold, *Chem. Soc. Rev.*, 2017, **46**, 1772–1784.

23 K. Honkala, *Surf. Sci. Rep.*, 2014, **69**, 366–388.

24 J. Carrasco, N. Lopez and F. Illas, *Phys. Rev. Lett.*, 2004, **93**, 225502.

25 J. Haubrich, E. Kaxiras and C. M. Friend, *Chem. - A Eur. J.*, 2011, **17**, 4496–4506.

26 A. R. Albuquerque, A. Bruix, I. M. G. Dos Santos, J. R. Sambrano and F. Illas, *J. Phys. Chem. C*, 2014, **118**, 9677–9689.

27 M. Rellán-Piñeiro and N. López, *J. Phys. Chem. Lett.*, 2018, **9**, 2568–2573.

28 M. Gerosa, C. E. Bottani, L. Caramella, G. Onida, C. Di Valentin and G. Pacchioni, *J. Chem. Phys.*, 2015, **143**, 134702.

29 C. F. Dickens and J. K. Nørskov, *J. Phys. Chem. C*, 2017, **121**, 18516–18524.

30 H. Y. Su, X. Ma, K. Sun, C. Sun, Y. Xu and F. Calle-Vallejo, *Chem. Sci.*, 2020, **11**, 4119–4124.

31 Z. Helali, A. Jedidi, O. A. Syzgantseva, M. Calatayud and C. Minot, *Theor. Chem. Acc.*, 2017, **136**, 100.

32 V. Korpelin, M. M. Melander and K. Honkala, *J. Phys. Chem. C*, 2022, **126**, 933–945.

33 T. Toyao, Z. Maeno, S. Takakusagi, T. Kamachi, I. Takigawa and K. Shimizu, *ACS Catal.*, 2020, **10**, 2260–2297.

34 M. Erdem Günay and R. Yıldırım, *Catal. Rev.*, 2021, **63**, 120–164.

35 C. Wulf, M. Beller, T. Boenisch, O. Deutschmann, S. Hanf, N. Kockmann, R. Kraehnert, M. Oezaslan, S. Palkovits, S. Schimmler, S. A. Schunk, K. Wagemann and D. Linke, *ChemCatChem*, 2021, **13**, 3223–3236.

36 D. Zagorac, H. Muller, S. Ruehl, J. Zagorac and S. Rehme, *J. Appl. Crystallogr.*, 2019, **52**, 918–925.

37 Y. Xu, M. Yamazaki and P. Villars, *Jpn. J. Appl. Phys.*, 2011, **50**, 11RH02.

38 A. Jain, S. P. Ong, G. Hautier, W. Chen, W. D. Richards, S. Dacek, S. Cholia, D. Gunter, D. Skinner, G. Ceder and K. A. Persson, *APL Mater.*, 2013, **1**, 011002.

39 S. Curtarolo, W. Setyawan, S. Wang, J. Xue, K. Yang, R. H. Taylor, L. J. Nelson, G. L. W. Hart, S. Sanvito, M. Buongiorno-Nardelli, N. Mingo and O. Levy, *Comput. Mater. Sci.*, 2012, **58**, 227–235.

40 J. E. Saal, S. Kirklin, M. Aykol, B. Meredig and C. Wolverton, *JOM*, 2013, **65**, 1501–1509.

41 K. T. Winther, M. J. Hoffmann, J. R. Boes, O. Mamun, M. Bajdich and T. Bligaard, *Sci. Data*, 2019, **6**, 75.

42 L. Chanussot, A. Das, S. Goyal, T. Lavril, M. Shuaibi, M. Riviere, K. Tran, J. Heras-Domingo, C. Ho, W. Hu, A. Palizhati, A. Sriram, B. Wood, J. Yoon, D. Parikh, C. L. Zitnick and Z. Ulissi, *ACS Catal.*, 2021, **11**, 6059–6072.

43 G. Kresse and J. Furthmüller, *Phys. Rev. B - Condens. Matter Mater. Phys.*, 1996, **54**, 11169–11186.

44 G. Kresse and J. Furthmüller, *Comput. Mater. Sci.*, 1996, **6**, 15–50.

45 J. P. Perdew, A. Ruzsinszky, G. I. Csonka, O. A. Vydrov, G. E. Scuseria, L. A. Constantin, X. Zhou and K. Burke, *Phys. Rev. Lett.*, , DOI:10.1103/PhysRevLett.100.136406.

46 Y. Hinuma, H. Hayashi, Y. Kumagai, I. Tanaka and F. Oba, *Phys. Rev. B*, 2017, **96**, 094102.

47 Y. Hinuma, T. Toyao, T. Kamachi, Z. Maeno, S. Takakusagi, S. Furukawa, I. Takigawa and K. Shimizu, *J. Phys. Chem. C*, 2018, **122**, 29435–29444.

48 N. J. O'Connor, A. S. M. Jonayat, M. J. Janik and T. P. Senftle, *Nat. Catal.*, 2018, **1**, 531–

539.
49 R. T. Sanderson, *J. Chem. Educ.*, 1988, **65**, 227–231.
50 I. Tanaka, K. Tatsumi, M. Nakano, H. Adachi and F. Oba, *J. Am. Ceram. Soc.*, 2002, **85**, 68–74.
51 T. Yamamoto and T. Mizoguchi, *Ceram. Int.*, 2013, **39**, 287–292.
52 A. M. Deml, A. M. Holder, R. P. O'Hayre, C. B. Musgrave and V. Stevanović, *J. Phys. Chem. Lett.*, 2015, **6**, 1948–1953.
53 A. A. Emery and C. Wolverton, *Sci. Data*, 2017, **4**, 170153.
54 C. Linderälv, A. Lindman and P. Erhart, *J. Phys. Chem. Lett.*, 2018, **9**, 222–228.
55 Y. Hinuma, S. Mine, T. Toyao, T. Kamachi and K. Shimizu, *Phys. Chem. Chem. Phys.*, 2021, **23**, 23768–23777.
56 Q. Zhao, Z. Yan, C. Chen and J. Chen, *Chem. Rev.*, 2017, **117**, 10121–10211.
57 J. Hwang, R. R. Rao, L. Giordano, Y. Katayama, Y. Yu and Y. Shao-Horn, *Science (80-.).*, 2017, **358**, 751–756.
58 X. Liu, M. Wang, C. Zhou, W. Zhou, K. Cheng, J. Kang, Q. Zhang, W. Deng and Y. Wang, *Chem. Commun.*, 2017, **54**, 140–143.
59 J. Zhang, M. Zhang, S. Chen, X. Wang, Z. Zhou, Y. Wu, T. Zhang, G. Yang, Y. Han and Y. Tan, *Chem. Commun.*, 2019, **55**, 973–976.
60 X. Cui, P. Gao, S. Li, C. Yang, Z. Liu, H. Wang, L. Zhong and Y. Sun, *ACS Catal.*, 2019, **9**, 3866–3876.
61 M. Belkin, D. Hsu and P. P. Mitra, *Adv. Neural Inf. Process. Syst.*, 2018, **2018**-**Decem**, 2300–2311.
62 M. Belkin, D. Hsu, S. Ma and S. Mandal, *Proc. Natl. Acad. Sci. U. S. A.*, 2019, **116**, 15849–15854.
63 P. L. Bartlett, P. M. Long, G. Lugosi and A. Tsigler, *Proc. Natl. Acad. Sci. U. S. A.*, 2020, **117**, 30063–30070.
64 S. M. Lundberg and S. I. Lee, in *Advances in Neural Information Processing Systems*, 2017, pp. 4765–4774.
65 S. M. Lundberg, B. Nair, M. S. Vavilala, M. Horibe, M. J. Eisses, T. Adams, D. E. Liston, D. K. W. Low, S. F. Newman, J. Kim and S. I. Lee, *Nat. Biomed. Eng.*, 2018, **2**, 749–760.
66 Y. Hinuma, T. Kamachi, N. Hamamoto, M. Takao, T. Toyao and K. I. Shimizu, *J. Phys. Chem. C*, 2020, **124**, 10509–10522.
67 A. M. Deml, V. Stevanović, C. L. Muhich, C. B. Musgrave and R. O'Hayre, *Energy Environ. Sci.*, 2014, **7**, 1996–2004.
68 Y. Hinuma, S. Mine, T. Toyao, Z. Maeno and K. I. Shimizu, *Phys. Chem. Chem. Phys.*, 2021, **23**, 16577–16593.
69 L. Liu and A. Corma, *Chem. Rev.*, 2018, **118**, 4981−5079.
70 A. M. Alexander and J. S. J. Hargreaves, *Chem. Soc. Rev.*, 2010, **39**, 4388–4401.

71 J. S. J. Hargreaves, *Coord. Chem. Rev.*, 2013, **257**, 2015–2031.

72 H. Kageyama, K. Hayashi, K. Maeda, J. P. Attfield, Z. Hiroi, J. M. Rondinelli and K. R. Poeppelmeier, *Nat. Commun.*, 2018, **9**, 772.

73 Y. Yan, B. Xia, Z. Xu and X. Wang, *ACS Catal.*, 2014, **4**, 1693−1705.

74 W. Wan, B. M. Tackett and J. G. Chen, *Chem. Soc. Rev.*, 2017, **46**, 1807–1823.

75 T. N. Ye, S. W. Park, Y. Lu, J. Li, M. Sasase, M. Kitano, T. Tada and H. Hosono, *Nature*, 2020, **583**, 391–395.

76 P. Wang, W. Chen, F. K. Chiang, A. Iulian Dugulan, Y. Song, R. Pestman, K. Zhang, J. Yao, B. Feng, P. Miao, W. Xu and E. J. M. Hensen, *Sci. Adv.*, 2018, **4**, eaau2947.

77 S. Ramanathan and S. T. Oyama, *J. Phys. Chem.*, 1995, **99**, 16365–16372.

78 S. Eijsbouts, S. W. Mayo and K. Fujita, *Appl. Catal. A Gen.*, 2007, **322**, 58–66.

79 R. R. Chianelli, G. Berhault and B. Torres, *Catal. Today*, 2009, **147**, 275–286.

80 C. Copéret, D. P. Estes, K. Larmier and K. Searles, *Chem. Rev.*, 2016, **116**, 8463−8505.

81 Y. Kobayashi, Y. Tang, T. Kageyama, H. Yamashita, N. Masuda, S. Hosokawa and H. Kageyama, *J. Am. Chem. Soc.*, 2017, **139**, 18240−18246.

82 K. Ooya, J. Li, K. Fukui, S. Iimura, T. Nakao, K. Ogasawara, M. Sasase, H. Abe, Y. Niwa, M. Kitano and H. Hosono, *Adv. Energy Mater.*, 2021, **11**, 2003723.

83 R. Michalsky, A. M. Avram, B. A. Peterson, P. H. Pfromm and A. A. Peterson, *Chem. Sci.*, 2015, **6**, 3965–3974.

84 C. D. Zeinalipour-Yazdi, J. S. J. Hargreaves and C. R. A. Catlow, *J. Phys. Chem. C*, 2015, **119**, 28368−28376.

85 J. M. Gracia, F. F. Prinsloo and J. W. Niemantsverdriet, *Catal. Letters*, 2009, **133**, 257–261.

86 M. A. Petersen and W. J. Van Rensburg, *Top. Catal.*, 2015, **58**, 665–674.

87 B. Chen, D. Wang, X. Duan, W. Liu, Y. Li, G. Qian, W. Yuan, A. Holmen, X. Zhou and D. Chen, *ACS Catal.*, 2018, **8**, 2709−2714.

88 Y. Hinuma, T. Toyao, N. Hamamoto, M. Takao, K. Shimizu and T. Kamachi, *J. Phys. Chem. C*, 2020, **124**, 27621–27630.

89 M. Haruta, *Catal. Today*, 1997, **36**, 153–166.

90 H. J. Freund and G. Pacchioni, *Chem. Soc. Rev.*, 2008, **37**, 2224–2242.

91 E. D. Goodman, J. A. Schwalbe and M. Cargnello, *ACS Catal.*, 2017, **7**, 7156−7173.

92 I. Ro, J. Resasco and P. Christopher, *ACS Catal.*, 2018, **8**, 7368−7387.

93 S. Hu and W.-X. Li, *Science (80-.).*, 2021, **374**, 1360–1365.

94 T. W. van Deelen, C. Hernández Mejía and K. P. de Jong, *Nat. Catal.*, 2019, **2**, 955–970.

95 M. Haruta, *Faraday Discuss.*, 2011, **152**, 11–32.

96 Y. Suchorski, S. M. Kozlov, I. Bespalov, M. Datler, D. Vogel, Z. Budinska, K. M. Neyman and G. Rupprechter, *Nat. Mater.*, 2018, **17**, 519–522.

97 S. C. Ammal and A. Heyden, *J. Catal.*, 2013, **306**, 78–90.

98 M. H. Liu, Y. W. Chen, T. S. Lin and C. Y. Mou, *ACS Catal.*, 2018, **8**, 6862−6869.

99 L. Giordano, J. Goniakowski and G. Pacchioni, *Phys. Rev. B - Condens. Matter Mater. Phys.*, 2001, **64**, 075417.

100 K. Honkala and H. Hakkinen, *J. Phys. Chem. C*, 2007, **111**, 4319–4327.

101 S. C. Ammal and A. Heyden, *J. Chem. Phys.*, 2010, **10**, 164703.

102 P. Schlexer, D. Widmann, R. J. Behm and G. Pacchioni, *ACS Catal.*, 2018, **8**, 6513−6525.

103 K. Murata, Y. Mahara, J. Ohyama, Y. Yamamoto, S. Arai and A. Satsuma, *Angew. Chemie - Int. Ed.*, 2017, **56**, 15993–15997.

104 D. Albani, M. Capdevila-Cortada, G. Vilé, S. Mitchell, O. Martin, N. López and J. Pérez-Ramírez, *Angew. Chemie - Int. Ed.*, 2017, **56**, 10755 –10760.

105 J. Ye, C. Liu and Q. Ge, *J. Phys. Chem. C*, 2012, **116**, 7817–7825.

106 J. Ye, C. Liu, D. Mei and Q. Ge, *ACS Catal.*, 2013, **3**, 1296−1306.

107 M. S. Frei, M. Capdevila-Cortada, R. García-Muelas, C. Mondelli, N. López, J. A. Stewart, D. Curulla Ferré and J. Pérez-Ramírez, *J. Catal.*, 2018, **361**, 313–321.

108 N. Rui, Z. Wang, K. Sun, J. Ye, Q. Ge and C. jun Liu, *Appl. Catal. B Environ.*, 2017, **218**, 488–497.

109 M. S. Frei, C. Mondelli, R. García-Muelas, K. S. Kley, B. Puértolas, N. López, O. V. Safonova, J. A. Stewart, D. Curulla Ferré and J. Pérez-Ramírez, *Nat. Commun.*, 2019, **10**, 3377.

110 A. Bavykina, I. Yarulina, A. J. Al Abdulghani, L. Gevers, M. N. Hedhili, X. Miao, A. R. Galilea, A. Pustovarenko, A. Dikhtiarenko, A. Cadiau, A. Aguilar-Tapia, J. L. Hazemann, S. M. Kozlov, S. Oud-Chikh, L. Cavallo and J. Gascon, *ACS Catal.*, 2019, **9**, 6910–6918.

111 X. Jia, K. Sun, J. Wang, C. Shen and C. jun Liu, *J. Energy Chem.*, 2020, **50**, 409–415.

112 P. Mehta, J. Greeley, W. N. Delgass and W. F. Schneider, *ACS Catal.*, 2017, **7**, 4707–4715.

113 K. B. S. Kumar, T. N. Whittaker, C. Peterson, L. C. Grabow and B. D. Chandler, *J. Am. Chem. Soc.*, 2020, **142**, 5760−5772.

114 A. R. Puigdollers and G. Pacchioni, *ChemCatChem*, 2017, **9**, 1119–1127.

115 P. Schlexer, A. Ruiz Puigdollers and G. Pacchioni, *Top. Catal.*, 2019, **62**, 1192–1201.

116 A. S. Bazhenov, M. M. Kauppinen and K. Honkala, *J. Phys. Chem. C*, 2018, **122**, 6774–6778.

117 A. Walsh and A. Zunger, *Nat. Mater.*, 2017, **16**, 964–967.

118 P. S. Lamoureux, K. Winther, J. A. Garrido Torres, V. Streibel, M. Zhao, M. Bajdich, F. Abild-Pedersen and T. Bligaard, *ChemCatChem*, 2019, **11**, 3581–3601.

119 G. H. Gu, C. Choi, Y. Lee, A. B. Situmorang, J. Noh, Y. H. Kim and Y. Jung, *Adv. Mater.*, 2020, **32**, 1907865.

120 J. Westermayr, M. Gastegger, K. T. Schütt and R. J. Maurer, *J. Chem. Phys.*, , DOI:10.1063/5.0047760.